Intermetallics 19 (2011) 698–706

Contents lists available at ScienceDirect

Intermetallics

journal homepage: www.elsevier.com/locate/intermet

Mechanical properties of $Nb_{25}Mo_{25}Ta_{25}W_{25}$ and $V_{20}Nb_{20}Mo_{20}Ta_{20}W_{20}$ refractory high entropy alloys

O.N. Senkov [a,b,*], G.B. Wilks [a,c], J.M. Scott [a,b], D.B. Miracle [a]

[a] Air Force Research Laboratory, Materials and Manufacturing Directorate, Wright-Patterson Air Force Base, OH 45433, USA
[b] UES, Inc., Dayton, OH 45432, USA
[c] General Dynamics Corporation, Dayton, OH 45431, USA

ARTICLE INFO

Article history:
Received 10 November 2010
Received in revised form
7 January 2011
Accepted 20 January 2011
Available online 18 February 2011

Keywords:
A. Intermetallics, miscellaneous
B. Mechanical properties at high temperatures
Mechanical properties at ambient temperature
D. Microstructure (as-cast, deformation-induced, recrystallization-induced)

ABSTRACT

Two refractory high entropy alloys with compositions near $Nb_{25}Mo_{25}Ta_{25}W_{25}$ and $V_{20}Nb_{20}Mo_{20}Ta_{20}W_{20}$, were produced by vacuum arc-melting. Despite containing many constituents, both alloys had a single-phase body-centered cubic (BCC) structure that remained not only stable after exposure to 1400 °C, but also disordered, as confirmed by the absence of superlattice reflections in neutron diffraction data. Compressive flow properties and microstructure development of these alloys were determined from room temperature up to 1600 °C. Limited compressive plasticity and quasi-cleavage fracture at room temperature suggest that the ductile-to-brittle transition for these alloys occurs above room temperature. At 600 °C and above, both alloys showed extensive compressive plastic strain. The yield stress of both alloys dropped by 30–40% between room temperature and 600 °C, but was relatively insensitive to temperature above 600 °C, comparing favorably with conventional superalloys.

© 2011 Elsevier Ltd. All rights reserved.

1. Introduction

Within the past several years, a novel alloying concept, based on achieving a high entropy of mixing between alloying elements, has been proposed [1–4]. According to this experimentally supported concept, the high entropy of mixing for different metallic elements (generally ≥5) of near equimolar concentrations can considerably decrease the Gibbs free energy and stabilize solid-solution-like phases with relatively simple crystal structures over competing complex and often brittle intermetallic phases. A number of these high entropy alloys (HEAs) have been developed for both functional and structural applications, and have demonstrated favorable combinations of strength, ductility, oxidation resistance, and thermal stability [3,5]. To date, HEA research has emphasized systems based on the late transition metals such as Cr, Mn, Fe, Co, Ni and Cu. Since metallic alloys for high-temperature load-bearing structures and thermal protection systems remain in high demand for aerospace applications, there is a clear rationale for also exploring HEAs composed of constituents with high melting temperatures. In response to this need, two refractory high entropy alloys, $Nb_{25}Mo_{25}Ta_{25}W_{25}$ and $V_{20}Nb_{20}Mo_{20}Ta_{20}W_{20}$, were successfully produced by vacuum arc melting [6]. In the as-solidified condition, these alloys had a dendritic, equiaxed grain microstructure consisting entirely of a single-phase body-centered cubic (BCC) crystal structure with lattice parameters and alloy densities equal to the average of the same parameters in elemental constituents. A very high microhardness of $H_v = 4.46$ GPa and 5.42 GPa were reported for the $Nb_{25}Mo_{25}Ta_{25}W_{25}$ and $V_{20}Nb_{20}Mo_{20}Ta_{20}W_{20}$, respectively [6]. The aim of this study is to expand on the previous work by assessing the mechanical behavior of these refractory alloys over a wide temperature range and gauging their properties relative to superalloys currently used for thermal protection systems and/or gas turbine engines.

2. Experimental procedures

$Nb_{25}Mo_{25}Ta_{25}W_{25}$ and $V_{20}Nb_{20}Mo_{20}Ta_{20}W_{20}$ alloys, referred to as Alloy 1 and Alloy 2, respectively, were prepared at Pittsburgh Materials Technology, Inc. (Jefferson Hills, PA) by vacuum arc melting of equimolar mixtures of the corresponding elements. High purity Ti was used as a getter for residual gases in a high vacuum chamber. W, Mo, and V were in the form of 45.7 mm diameter rods with a purity of 99.7%, 99.0%, and 99.9% (by weight), respectively, while Ta and Nb were in the form of chips and had a purity of 99.0%

* Corresponding author. UES, Inc., Dayton, OH 45432, USA. Tel.: +1 937 2551320.
E-mail address: oleg.senkov@wpafb.af.mil (O.N. Senkov).

0966-9795/$ – see front matter © 2011 Elsevier Ltd. All rights reserved.
doi:10.1016/j.intermet.2011.01.004

and 99.99%, respectively. The alloys were prepared in the form of buttons of ~10 mm thick and ~60–70 mm in diameter. To achieve a homogeneous distribution of elements in the alloys, the buttons were re-melted four times, flipped for each melt, and had a total time of over 1 h in the liquid state. The buttons had lustrous surfaces indicating that no substantial oxidation occurred during vacuum arc melting. The final near-equiatomic compositions of the alloys, determined by inductively-coupled plasma-optical emission spectroscopy (ICP-OES), are reported in Table 1

Neutron diffraction of the alloys in as-solidified and annealed (1400 °C for 19 h) conditions was conducted at the NIST Center for Neutron Research using a high resolution powder diffractometer BT1 (Dr. Mark Green, Instrument Scientist). A Cu(311) monochromator was used, which produces neutrons with a wavelength of 1.5401 Å. The maximum beam size was 15 mm × 50 mm. Prior to neutron exposure, the alloy samples (10 g each) were crushed into powder and loaded into 9.2 mm diameter cylindrical vanadium cans. 32 Helium-3 detectors located at 5° intervals collected scattered neutrons in the 2Θ scan range from 0° to 167°. The CMPR program [7] was used for peak fitting and indexing of neutron diffraction data.

Microstructures of as-solidified and deformed samples were analyzed using a scanning electron microscope (SEM) equipped with a backscatter electron (BSE) detector. Cylindrical specimens for compression testing were electric-discharged machined from the cast buttons. The sample axis was perpendicular to the button surface that was in contact with the copper mold during solidification. The samples were 3.6 mm in diameter and 5.4 mm in height giving an aspect ratio of 1.5. The compression faces of the samples were paralleled by mechanical polishing and lubricated with boron nitride for elevated temperature tests. Compression tests were conducted at 600 °C, 800 °C, 1000 °C, 1200 °C, 1400 °C and 1600 °C in a computer-controlled Instron (Instron, Norwood, MA) mechanical testing machine outfitted with a Brew vacuum furnace and silicon carbide platens. Prior to each test, the furnace chamber was evacuated to 10^{-6} torr. The sample was then heated to the test temperature in 45–60 min and soaked at temperature for 15 min under 5 N load control, and then compressed to fracture or to a 40% height reduction, whichever occurred first, at a constant ram speed that provided an initial strain rate of 0.001 s^{-1}. Room temperature compression tests were conducted on the same Instron machine, with the same platen setup and at the same strain rate conditions, but in air, and a thin (~50 μm) Teflon foil was used as a lubricating material between the die and sample contacting surfaces. Displacement in all tests was monitored and synced with load output from the test frames using a Video Displacement and Image Correlation System from Correlated Solutions Inc, which also provided a visual record of individual specimen deformation response.

3. Results and discussion

3.1. Mechanical properties

3.1.1. $Nb_{25}Mo_{25}Ta_{25}W_{25}$ Alloy

Compressive engineering stress vs. engineering strain curves for the $Nb_{25}Mo_{25}Ta_{25}W_{25}$ alloy are illustrated in Fig. 1. During testing at room temperature (RT, 23 °C), the alloy yielded at $\sigma_{0.2} = 1058$ MPa,

Table 1
Chemical composition (in wt.%/at.%) of two refractory alloys produced by vacuum arc melting.

Alloy ID/Element	W	Nb	Mo	Ta	V
Alloy 1	36.0/27.3	15.2/22.7	17.8/25.6	31.7/24.4	0.0/0.0
Alloy 2	33.0/21.1	16.2/20.6	17.6/21.7	23.9/15.6	9.08/21.0

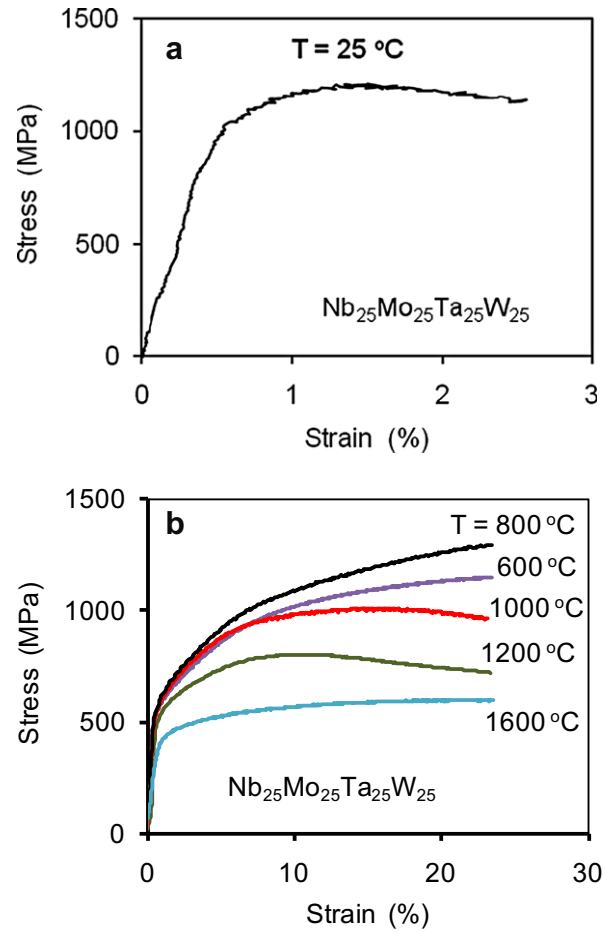

Fig. 1. Compressive engineering stress–strain curves for the $Nb_{25}Mo_{25}Ta_{25}W_{25}$ alloy obtained at (a) room temperature and (b) elevated temperatures.

showed a maximum strength, σ_m, of 1211 MPa at $\varepsilon_p = 0.95\%$, and failed by splitting at $\varepsilon_p = 2.1\%$ (Fig. 1a). Here ε_p is the plastic strain, $\sigma_{0.2}$ is the yield stress at $\varepsilon_p = 0.2\%$. After correcting for machine compliance, the compression modulus, E_{comp}, was determined to be $E_{comp} = 220 \pm 20$ GPa. This resulted in the total elastic strain, ε_e, just before the fracture, of $\varepsilon_e = 0.52\%$ and an accumulated elastic energy per unit volume $W = 2970 \pm 270$ kJ/m^3.

Samples deformed at $T = 600$ °C and 800 °C showed continuous strengthening after yield at $\sigma_{0.2} = 561$ MPa and 552 MPa, respectively (Fig. 1b). The strengthening rate and flow stress at 800 °C were higher than at 600 °C. The samples deformed at 1000 °C, 1200 °C and 1400 °C reached a peak stress at an intermediate strain, which decreased from ~15% to ~5% with an increase in the temperature, and then their strength continuously decreased. The apparent strain softening at these temperatures was probably a manifestation of plastic instability and spallation of the specimen surface material observed at higher strains, because the reduced cross-sectional area cannot be correctly accounted for in the depicted engineering stress–strain plot [8]. Samples deformed at 1600 °C, showed almost steady state flow at a constant stress of ~590–600 MPa, and no surface spallation occurred at this temperature. While flow behavior after peak stress in some conditions was sensitive to the plastic instability and failure mode, the authors do not believe that this significantly affected the assessment of yield stress in any condition. Consequently, the yield stress for this material steadily decreased as a function of temperature from 548 MPa at 1000 °C to 405 MPa at 1600 °C (Table 2).

Table 2
Compression properties of the $Nb_{25}Mo_{25}Ta_{25}W_{25}$ alloy.

Temperature °C	Yield stress MPa	Peak stress MPa	Peak strain %	Stress at 25% MPa
23	1058	1211	1.5	1135[a]
600	561	–	–	1140
800	552	–	–	1283
1000	548	1008	16	763
1200	506	803	12	725
1400	421	467	9	331
1600	405	600	27	597

[a] Room temperature fracture stress. Fracture occurs at $\varepsilon = 2.6\%$.

Table 3
Compression properties of the $V_{20}Nb_{20}Mo_{20}Ta_{20}W_{20}$ alloy.

Temperature °C	Yield stress MPa	Peak stress MPa	Peak strain %	Fracture stress MPa	Fracture strain %
23	1246	1270	0.5	1087	1.7
600	862	1597	13	1597	13
800	846	1536	16	1509	17
1000	842	1454	14	1370	19
1200	735	943	4.2	802	7.5
1400	656	707	1.6	–	–
1600	477	479	0.95	–	–

3.1.2. $V_{20}Nb_{20}Mo_{20}Ta_{20}W_{20}$ alloy

Compressive engineering stress–strain curves for the $V_{20}Nb_{20}Mo_{20}Ta_{20}W_{20}$ alloy are shown in Fig. 2. At rt (Fig. 2a), the alloy showed a yield stress $\sigma_{0.2} = 1246$ MPa and a maximum (peak) stress strength of $\sigma_m = 1270$ MPa, while failing at $\varepsilon_p = 1.7\%$ by the same splitting mechanism observed in the 4-component alloy. The compression modulus was $E_{comp} = 180 \pm 15$ GPa, which resulted in $\varepsilon_e \approx 0.60\%$ and $W = 3260 \pm 330$ kJ/m^3 at the fracture point ($\sigma_f = 1087$ MPa). An increase in temperature to 600 °C decreased the yield stress to $\sigma_{0.2} = 862$ MPa, but increased total compressive failure strain to $\varepsilon_f \approx 13\%$ (Fig. 2b and Table 3). With a further increase in the temperature to 1000 °C, $\sigma_{0.2}$ slightly decreased to 842 MPa and ε_f increased to 19%. Up to a strain of ~5–7%, the deformation response of the samples deformed at 600 °C, 800 °C and 1000 °C were almost identical, however, σ_m continuously decreased from 1597 MPa to 1454 MPa.

An increase in the temperature to 1200 °C led to a noticeable decrease in $\sigma_{0.2}$ (to 735 MPa), ε_f (to ~8%), and σ_m, (to 943 MPa) (see Fig. 2b). Further increases in temperature to 1400 °C and 1600 °C led to a rapid decline in yield stress and apparent softening. As with the 4-element system this apparent softening was accompanied with spallation of material from the side surfaces of deforming specimens. Again, the authors are confident that while the spallation of material in these conditions obviates an analysis of post-yield strain-hardening behavior, the yield stress in these conditions is still representative of the intrinsic properties of the material. The results of compression testing of the $V_{20}Nb_{20}Mo_{20}Ta_{20}W_{20}$ alloy are summarized in Table 3.

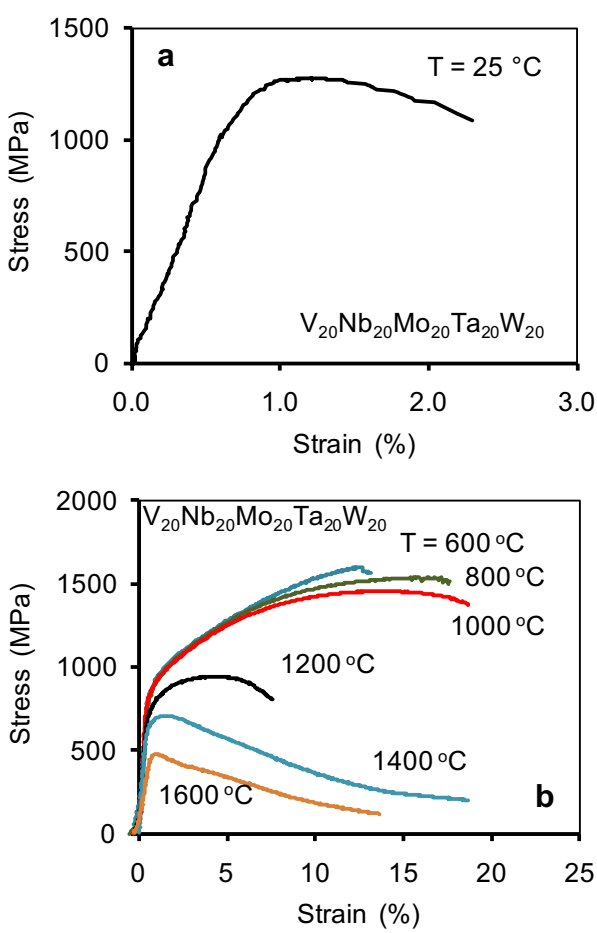

Fig. 2. Compressive engineering stress–strain curves for the $V_{20}Nb_{20}Mo_{20}Ta_{20}W_{20}$ alloy obtained at (a) room temperature and (b) elevated temperatures.

3.1.3. Comparison with superalloys

Fig. 3 shows the temperature dependence of the yield stress (YS) of the studied HEAs and two Ni-based superalloys, Inconel 718 [9] and Haynes 230 [10]. Inconel 718, which composition is given in Table 4, is a heat treatable alloy and the YS values shown in Fig. 3 correspond to heat treatment, which includes annealing at 982 °C for1 h, aging at 718 °C for 8 h, additional aging at 621 °C for 18 h followed by an air cool. After this heat treatment, the YS exceeds 1000 MPa at temperatures up to 650 °C. However, the YS of Inconel 718 rapidly decreases to 138 MPa with a further increase in temperature to 982 °C, while melting occurs at ~1210 °C. Inconel 718 is generally used in gas turbine engines with operating temperatures not exceeding 800 °C.

Another superalloy, Haynes 230, has a considerably lower YS, which, however, is almost constant, ~255–275 MPa, in the

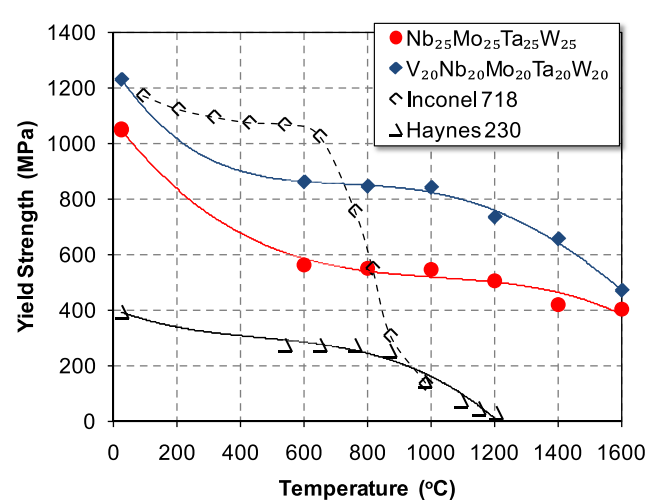

Fig. 3. The temperature dependence of the yield stress of $Nb_{25}Mo_{25}Ta_{25}W_{25}$ and $V_{20}Nb_{20}Mo_{20}Ta_{20}W_{20}$ HEAs and two superalloys, Inconel 718 [9] and Haynes 230 [10].

Table 4
Composition (in wt.%) of Inconel 718 [9].

Ni	Cr	Fe	Mo	Nb	Al	Ti	Co[a]	Mn[a]	Cu[a]	Si[a]	C[a]	S[a]	P[a]	B[a]
52	19	Bal.	3.0	5.1	0.9	0.3	1.0	0.35	0.5	0.35	0.08	0.015	0.015	0.006

[a] Maximum.

temperature range from 540 °C to 870 °C. This alloy, which composition is given in Table 5, is non-heat treatable and its applications include hot section components with low loads, such as combustion cans, thermocouple protection tubes, heat exchangers and industrial furnace fixtures, muffles and thermal protection systems operating at temperatures up to 1100 °C.

The yield stress values of the refractory HEAs are much higher than those of Haynes 230 at all studied temperatures and higher than those of Inconel 718 at temperatures above 800 °C (see Fig. 3). Moreover, the decrease in the YS of these HEAs in the temperature range from 600 °C to 1600 °C is rather weak. For example, YS decreases from 561 to 405 MPa for the $Nb_{25}Mo_{25}Ta_{25}W_{25}$ alloy and from 862 to 470 MPa for the $V_{20}Nb_{20}Mo_{20}Ta_{20}W_{20}$ alloy in this temperature range. Even after normalizing stresses by densities of the appropriate alloys, the two high entropy alloys still have normalized yield stress that are more than twice (for the $Nb_{25}Mo_{25}Ta_{25}W_{25}$ alloy) or four times (for the $V_{20}Nb_{20}Mo_{20}Ta_{20}W_{20}$ alloy) higher than for Inconel 718 or Haynes 230 at 1000 °C.

The strong resistance to high-temperature softening, as compared to the superalloys, is likely due to slow diffusion of elements in the refractory HEAs at temperatures up to 1600 °C, which directly relates to high melting points, T_m, of these alloys. Indeed, a rapid decrease in strength of conventional alloys and superalloys generally occurs at temperatures above $T_r \sim 0.6T_m$, where T_m is given in degrees K [11,12]. The rule-of-mixtures estimates of T_m for the $Nb_{25}Mo_{25}Ta_{25}W_{25}$ (T_m = 3177 K) and $V_{20}Nb_{20}Mo_{20}Ta_{20}W_{20}$ (T_m = 2946 K) alloys [6] give T_r = 1633 °C and T_r = 1495 °C, respectively. These estimates also explain a noticeable drop in the yield stress of the $V_{20}Nb_{20}Mo_{20}Ta_{20}W_{20}$ alloy at 1600 °C (see Fig. 3).

3.2. Microstructure

3.2.1. Crystal structure

Neutron diffraction analysis of both as-solidified refractory high entropy alloys indicates the presence of a single-phase BCC crystal structure, which was retained after annealing at 1400 °C for 19 h (Fig. 4). In the $Nb_{25}Mo_{25}Ta_{25}W_{25}$ alloy, the lattice parameter was determined to be a = 3.220 Å, both in as-solidified and annealed conditions. In the $V_{20}Nb_{20}Mo_{20}Ta_{20}W_{20}$ alloy, a = 3.185 Å in the as-solidified condition and a = 3.187 Å in the annealed condition. These results indicate that the BCC crystal structure formed in both alloys during solidification is stable upon heating at least up to 1400 °C. Moreover, even after being subject to elevated temperatures, there appears to be no strong evidence for an order–disorder transition in either alloy, as can be seen from the absence of superlattice reflections in the reported diffraction patterns. Although unlikely, it should be noted that some ordering of vanadium in alloy 2 could be possible given the inability to detect superlattice reflections due to its low coherent neutron scattering cross-section [13].

Table 5
Composition (in wt.%) of Haines 230 [10].

Ni[a]	Cr	Fe[b]	Mo	W	Co[b]	Mn	Al	Si	C	La	B[b]
57	22	3	2	14	5	0.5	0.3	0.4	0.1	0.02	0.015

[a] As balance.
[b] Maximum.

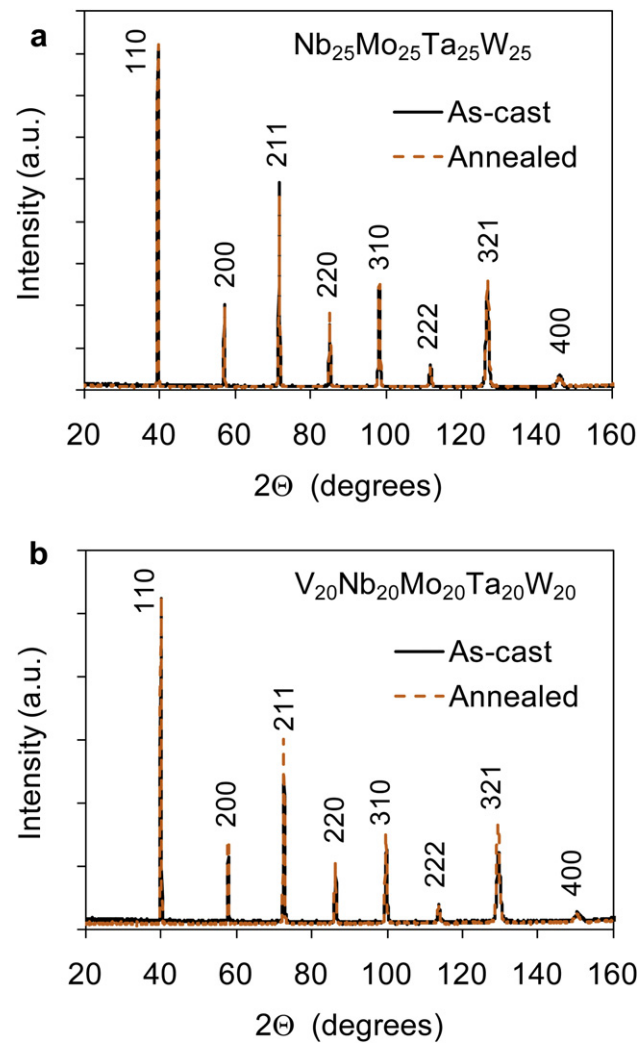

Fig. 4. Neutron diffraction patterns of (a) $Nb_{25}Mo_{25}Ta_{25}W_{25}$ and (b) $V_{20}Nb_{20}Mo_{20}Ta_{20}W_{20}$ in as-solidified and annealed (1400 °C for 19 h) conditions. The wavelength is 1.5401 Å.

3.2.2. Microstructure in as-solidified condition

SEM backscatter electron images of the refractory high entropy alloys in the as-solidified condition are shown in Fig. 5. The average grain size in the $Nb_{25}Mo_{25}Ta_{25}W_{25}$ alloy was 200 μm, although low magnification images through the cross-section of the cast button reveal a non-uniform grain size distribution, with larger grains in the regions experiencing slower cooling during solidification, i.e. near the surfaces not in contact with the water-cooled copper plate (Fig. 5a). The $V_{20}Nb_{20}Mo_{20}Ta_{20}W_{20}$ alloy had a much finer grain size, on the order of 80 μm, although it was also clearly sensitive to cooling rate during solidification (Fig. 5b). Higher magnification images reveal a dendritic structure in both alloys (Fig. 5c and d). Uneven Z-contrast inside the grains indicates slightly different compositions of dendritic and interdendritic regions due to constitutional segregation during solidification [6]. The lighter Z-contrast in both materials indicates that the dendrite arms were enriched with heavier elements than the interdendritic regions. The dendrite arm spacing was the same in both alloys, ~20–30 μm, as expected from the similar solidification conditions.

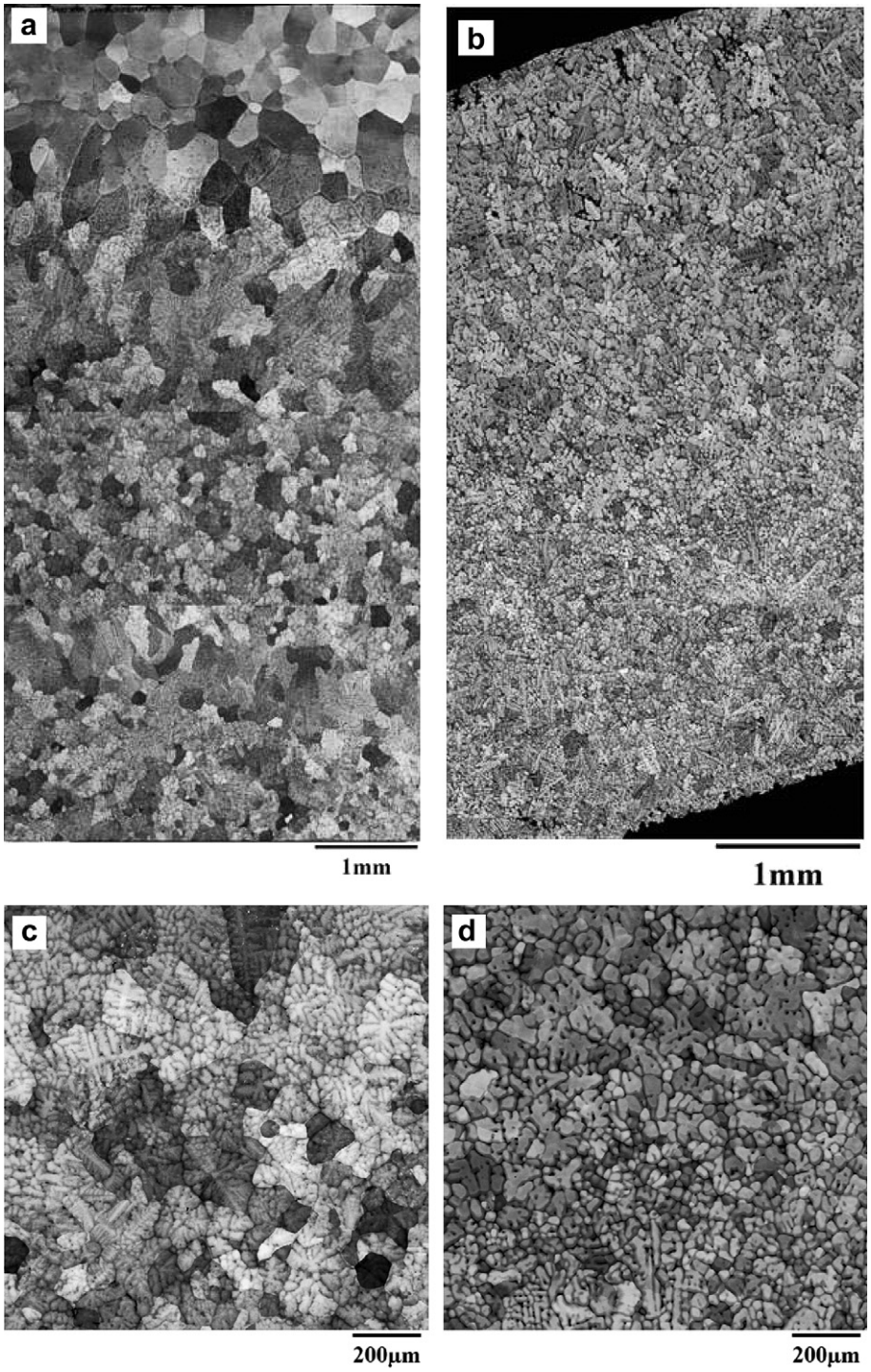

Fig. 5. Backscatter electron images of polished cross-sections of (a,c) $Nb_{25}Mo_{25}Ta_{25}W_{25}$ and (b,d) $V_{20}Nb_{20}Mo_{20}Ta_{20}W_{20}$ alloys.

3.2.3. Fractography of samples deformed at room temperature

The high entropy alloy samples deformed at room temperature fractured by splitting along surfaces nearly parallel to the compression direction. Typical SEM images of the fracture surfaces are shown in Fig. 6, in which brittle quasi-cleavage fracture is evident for both alloys. At low magnification, a faceted appearance of the fracture is visible in both alloys (Fig. 6a, b). The size of these facets is finer for the V-containing alloy, an observation consistent with the smaller average grain size of this alloy and the apparent fracture mode, since during quasi-cleavage it would be expected that the crack-growth direction would change on intercepting grain or subgrain boundaries. Higher magnification images illustrate characteristics of the quasi-cleavage fracture, such as flat facets, angular faceted steps, river-pattern markings, cleavage feathers and tongues (Fig. 6c–f). There are indications that pores are participating in fracture, but it is not clear that they initiate fracture. Nevertheless, this fracture by splitting suggests that the primary failure mode is tensile not shear, and that the brittle-to ductile transition temperature (DBTT) is clearly above room temperature for these BCC materials.

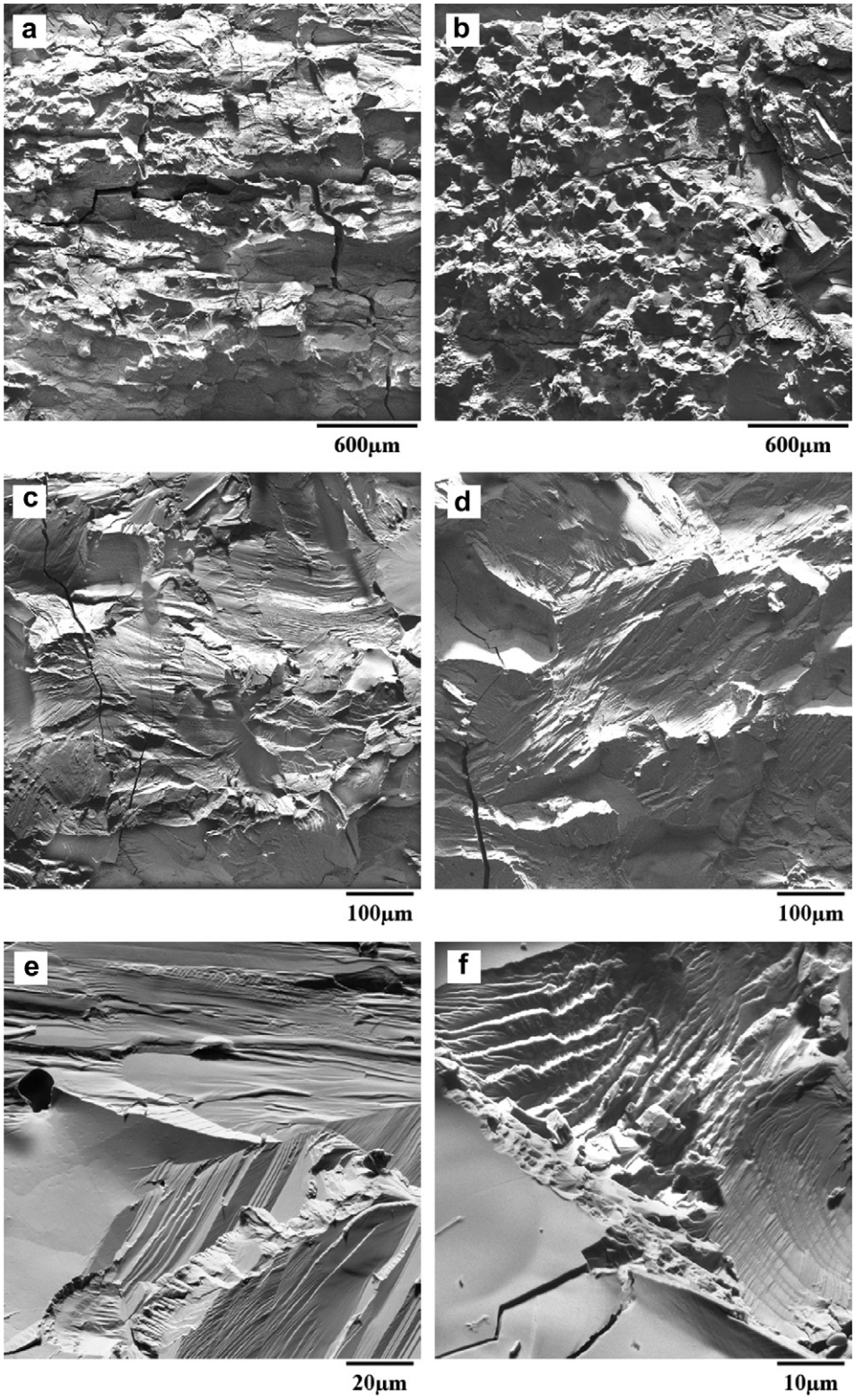

Fig. 6. SEM images of fracture surfaces of (a,c,e) $Nb_{25}Mo_{25}Ta_{25}W_{25}$ and (b,d,f) $V_{20}Nb_{20}Mo_{20}Ta_{20}W_{20}$ alloys after compression deformation at 25 °C.

3.2.4. Microstructure after deformation at 800 °C

SEM backscatter electron images of the samples deformed at 800 °C are depicted in Fig. 7. Lower magnification images of the cross-sections reveal different deformation behavior in the $Nb_{25}Mo_{25}Ta_{25}W_{25}$ and $V_{20}Nb_{20}Mo_{20}Ta_{20}W_{20}$ alloy samples. Specifically, the $Nb_{25}Mo_{25}Ta_{25}W_{25}$ alloy showed a more ductile behavior as it fractured due to localized shear and cracking along a direction inclined ~40° to the loading direction (Fig. 7a). Grains inside the shear region were heavily deformed, while no noticeable changes in the grain/dendritic structure (relative to the as-solidified condition) were seen in other regions of the deformed sample (Fig. 7c). On the other hand, the $V_{20}Nb_{20}Mo_{20}Ta_{20}W_{20}$ alloy experienced much

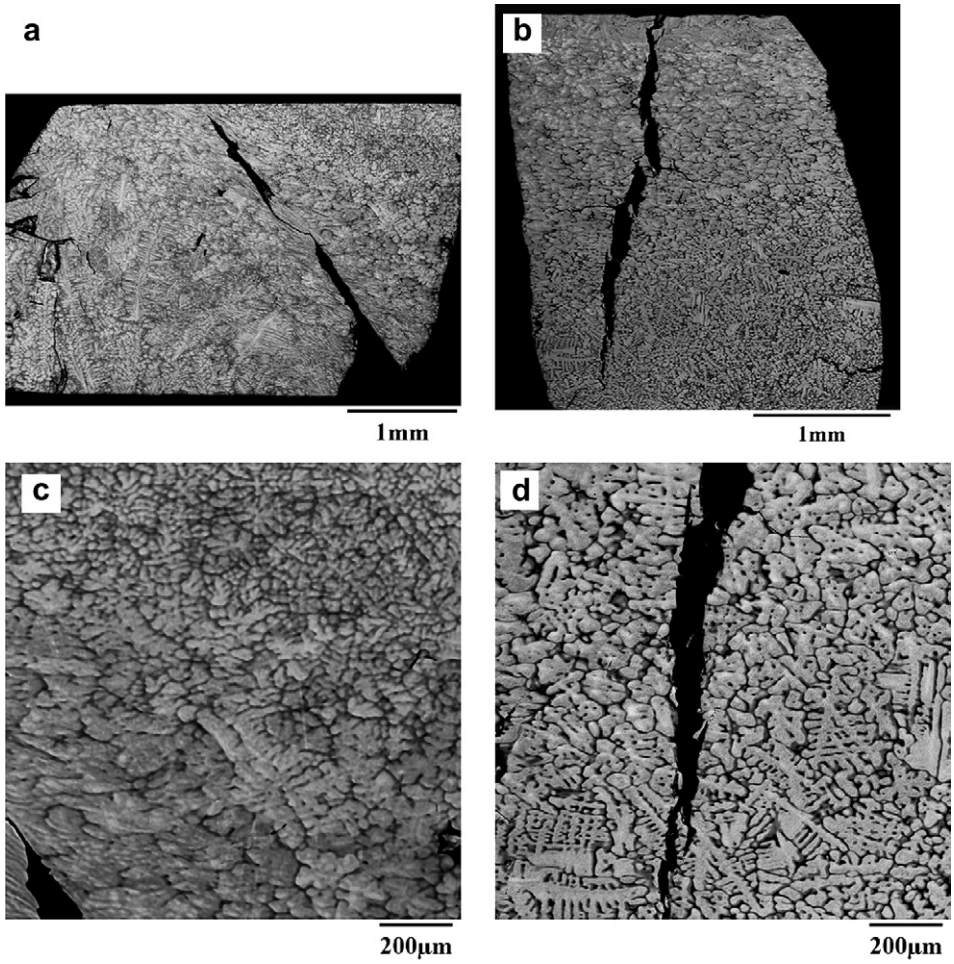

Fig. 7. SEM backscatter electron images of the (a,c) $Nb_{25}Mo_{25}Ta_{25}W_{25}$ and (b,d) $V_{20}Nb_{20}Mo_{20}Ta_{20}W_{20}$ alloys after compression deformation at 800 °C. Depicted cross-sections are parallel to the loading direction (vertical) and located half-way between the surface and center of the samples.

smaller plastic strain, and its fracture occurred by crack propagation along a direction inclined 10° relative to the loading axis, with strong participation of grain boundaries during crack growth (Fig. 7b, d). No noticeable evidence of grain deformation was observed; however, the grain size slightly increased (to about 100–120 μm) in this alloy (Fig. 7d). The dendritic structure was retained in both materials.

3.2.5. Microstructure after deformation at 1400 °C

After deformation at 1400 °C of the $Nb_{25}Mo_{25}Ta_{25}W_{25}$ sample, large grains compressed along the loading direction are clearly seen, both at low and high magnifications (Fig. 8a and b). Grains were considerably larger (~300 μm) than in the non-deformed condition indicating a combination of temperature and strain-induced grain growth. Dendrite arms had the tendency to align perpendicular to the loading direction (Fig. 8b), which can be an indication of grain rotations and grain boundary sliding. Voids located along grain boundaries also point to grain boundary sliding during compression of this alloy sample.

In contrast, no evidence of grain compression was seen on images of the $V_{20}Nb_{20}Mo_{20}Ta_{20}W_{20}$ alloy sample deformed at 1400 °C (Fig. 8c and d). Grains remained equiaxed throughout the sample cross-section although their size considerably increased to ~150 μm. The equiaxed morphology of grains can be an indication of dynamic recrystallization occurring in this alloy sample during compression at 1400 °C. Considerable strain softening (see Fig. 2) is another evidence of dynamic recrystallization in the $V_{20}Nb_{20}Mo_{20}Ta_{20}W_{20}$ alloy under these loading conditions [12], although material spallation from the side surfaces of deforming samples can also take part in the apparent stress decrease, as it was discussed in Section 3.1.

It is interesting to note that the dendritic structure was still present after deformation of both alloys at 1400 °C. Even dynamic recrystallization was not able to remove the compositional inhomogeneity. This result supports earlier observations [3,5,14] of strongly reduced diffusivity of elements in high entropy alloys.

4. Summary and conclusions

The phase stability, microstructure development, and mechanical behavior of two refractory high entropy alloys, $Nb_{25}Mo_{25}Ta_{25}W_{25}$ and $V_{20}Nb_{20}Mo_{20}Ta_{20}W_{20}$ were investigated from room temperature up to 1600 °C. Neutron diffraction analysis in material tested at room temperature and annealed at 1400 °C indicated that both alloys had a single-phase, BCC crystal structure. The lattice parameter for the 4-element alloy was $a = 3.220$ Å, both in as-solidified and annealed conditions. The 5-element alloy had a lattice parameter $a = 3.185$ Å in the as-solidified condition and $a = 3.187$ Å in the annealed condition. No superlattice reflections were observed at either temperature confirming that both alloys were disordered and lacked an order–disorder transition or other instability over the studied temperature range.

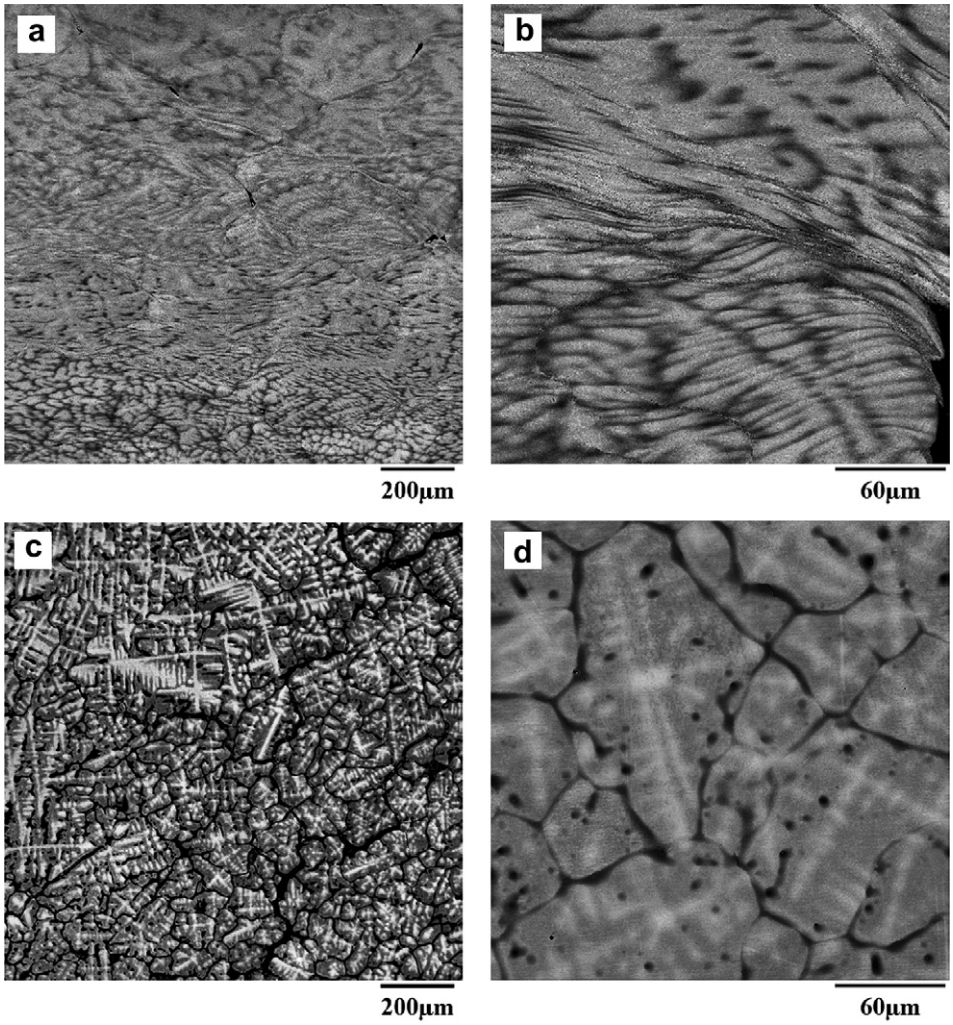

Fig. 8. SEM backscatter images of the (a,b) $Nb_{25}Mo_{25}Ta_{25}W_{25}$ and (c,d) $V_{20}Nb_{20}Mo_{20}Ta_{20}W_{20}$ alloys after compressive deformation at 1400 °C. Depicted cross-sections are parallel to the loading direction (vertical) and located half-way between the surface and center of the samples.

During deformation at room temperature, the alloys showed high yield stress of 1058 MPa and 1246 MPa, but a limited ductility of about 2.0% and 1.5% of plastic strain, for the $Nb_{25}Mo_{25}Ta_{25}W_{25}$ and $V_{20}Nb_{20}Mo_{20}Ta_{20}W_{20}$ alloys, respectively. Quasi-cleavage fracture by splitting along the surfaces that were almost parallel to the compression direction, suggests that fracture occurred under tensile stresses and that the brittle-to ductile transition temperature for these BCC refractory alloys is above room temperature.

Over the temperature range of 600 °C–1000 °C, both alloys demonstrated good plastic flow with compressive strain exceeding 10–15% prior to localized shear accompanied by a drop in strength, suggesting that the DBTT for each alloy is located between room temperature and 600 °C. In the $Nb_{25}Mo_{25}Ta_{25}W_{25}$ alloy, the yield stress was 561 MPa at 600 °C and it continuously decreased with temperature down to 405 MPa at 1600 °C. The $V_{20}Nb_{20}Mo_{20}Ta_{20}W_{20}$ alloy was ~200 MPa stronger in the temperature range of 600 °C – 1200 °C. However, the yield stress of the $V_{20}Nb_{20}Mo_{20}Ta_{20}W_{20}$ alloy decreased more rapidly than that of the $Nb_{25}Mo_{25}Ta_{25}W_{25}$ alloy in the temperature range of 1200 °C – 1600 °C, so that its yield stress at 1600 °C (477 MPa) was close to that of the $Nb_{25}Mo_{25}Ta_{25}W_{25}$ alloy (405 MPa).

While near-steady state flow occurred at 1200–1600 °C in the $Nb_{25}Mo_{25}Ta_{25}W_{25}$ alloy, the $V_{20}Nb_{20}Mo_{20}Ta_{20}W_{20}$ alloy showed considerable softening shortly after yielding in this temperature range. This apparent softening of the 5-element alloy was concomitant with material spallation from the side surfaces of deforming samples, obfuscating stress measurement during compression, and dynamic recrystallization. Microstructural examination of both materials indicated that grain boundary sliding occurred at these temperatures. It was responsible for void formation and fracture along grain boundaries. These observations, combined with the fact that the dendritic structure was retained even at 1400 °C, anecdotally support the concept that the high configurational entropy of these alloys is capable of strongly suppressing constituent diffusivity for accommodation of the grain-boundary sliding.

Acknowledgments

Discussions with Drs. Christopher F. Woodward, Patrick L. Martin and Young-Won Kim are greatly appreciated. The authors would like to acknowledge their appreciation of the technical support provided by S.V. Senkova (UES, Inc.) in microstructure analysis. The neutron diffraction was performed at the National Institute of Standard and Technology (Dr. Mark Green). This work was supported by the Air Force Office of Scientific Research (Dr.

Joan Fuller, Program Manager) and through USAF Contract No. FA8650-10-D-5226.

References

[1] Yeh JW, Chen SK, Lin SJ, Gan JY, Chin TS, Shun TT, et al. Adv Eng Mater 2004;6(5):299–303.
[2] Huang PK, Yeh JW, Shun TT, Chen SK. Adv Eng Mater 2004;6(1–2):74–8.
[3] Yeh JW. Ann. Chim. Sci. Mat. 2006;31(6):633–48.
[4] Zhang Y, Zhou YJ, Lin JP, Chen GL, Liaw PK. Solid-solution phase formation rules for multi-component alloys. Adv Eng Mater 2008;10(6):534–8.
[5] Yeh J-W, Chen Y-L, Lin S-J, Chen S-K. Mater Sci Forum 2007;560:1–9.
[6] Senkov ON, Wilks GB, Miracle DB, Chuang CP, Liaw PK. Intermetallics 2010;18:1758–65.
[7] Toby BH. J Appl Crystallogr 2005;38:1040–1.
[8] Semiatin SL, Jonas JJ. Formability and workability of metals: plastic instability and flow localization. OH, USA: ASM, Metals Park; 1984.
[9] Inconel® Alloy 718, http://www.specialmetals.com/documents/Inconelalloy718.pdf.
[10] Haynes®230® Alloy, www.haynesintl.com/pdf/h3060.pdf.
[11] Dieter GE. Mechanical metallurgy. 3rd ed. New York: McGraw-Hill, Inc.; 1986.
[12] McQueen HJ, Jonas JJ. Treatise on materials science and technology. In: Plastic deformation of materials, vol. 6. New York: Academic Press; 1975. 393–493.
[13] NIST Neutron Scattering Lengths and Cross Sections, http://www.ncnr.nist.gov/resources/n-lengths/.
[14] Tsai M-H, Yeh J-W, Gan J-Y. Thin Solid Films 2008;516:5527–30.